Journal of ELECTRONIC MATERIALS, Vol. 48, No. 9, 2019
https://doi.org/10.1007/s11664-019-07137-2

Global Analysis of Influence of Contacts on Heusler-Based Thermoelectric Modules

G. ROY,[1,4] C. VAN DER REST,[1] S. HEYMANS,[1] E. QUINTIN,[1] V. DUPONT,[2] J.P. ERAUW,[2] A. SCHMITZ,[3] and P.J. JACQUES[1]

1.—Institute of Mechanics, Materials and Civil Engineering, Materials and Process Engineering (IMAP), Université catholique de Louvain, Place Sainte Barbe 2, 1348 Louvain-La-Neuve, Belgium. 2.—Belgian Ceramic Research Center (BCRC), avenue Gouverneur Cornez 4, 7000 Mons, Belgium. 3.—CRM Group, avenue du Bois Saint Jean 21, 4000 Liège, Belgium. 4.—e-mail: geoffrey.roy@uclouvain.be

Interest in waste heat recovery using thermoelectricity has increased in recent decades. To date, most such research and development has focused on high-performance and/or low-cost materials. However, for practical applications, modules based on these materials are needed. This work presents the development and optimization of modules based on the low-cost Fe_2VAl Heusler compound. It depicts a global analysis of the assembly in terms of the microstructure of the joint, the contact resistances, and the module performance. Based on this analysis, a generic method for developing joining solutions for new thermoelectric materials is proposed. Using this method, the diffusion bonding technique leading to electrical contact resistance of 5×10^{-9} Ω m^2 is highlighted and a thermoelectric module with power density above 500 W m^{-2} for a temperature difference of 200 K developed.

Key words: Thermoelectric module, Heusler, electrical contact, thermal contact

INTRODUCTION

In recent years, thermoelectric generators (TEGs) have attracted interest for use in waste heat harvesting. While most research has focused on optimization of material performance, major challenges remain at the level of the complete setup, which still limits the use of thermoelectricity to niche applications.[1] In particular, the assembly of the constitutive elements of the TEG, viz. *p*- and *n*-type materials, electrical and thermal conductors, and insulators, intrinsically leads to contact resistances that hinder the performance of the device.[2] As shown in Fig. 1, the contacts corresponding to each interface between different materials influence the electrical and/or thermal performance. Previous studies on thermoelectric contacts have mostly focused on either optimization of metal–semiconductor contacts (related to the microstructure of different types of thermoelectric materials[3–5]) or the influence of contact resistances at the system level,[6–11] which are only parts of the global issue. Recently, Ngan et al.[12] studied the relationship between contact resistance and microstructure. However, they only estimated theoretically the influence of this relationship on the system efficiency. To enable widespread use of new thermoelectric materials in practical applications, scaling up from a single contact to a complete TEG should be investigated experimentally. This step is mandatory to validate the repeatability and scalability of any joining method. It seems that none of these studies have proposed a global approach relating experimentally the microstructure of the joints to the contact resistance and the performance at the TEG level, even though such a global view could accelerate development of new optimized thermoelectric devices based on innovative materials.

The aim of the work presented herein is to apply such a global methodology to optimize a TEG based

(Received October 1, 2018; accepted March 12, 2019; published online April 1, 2019)

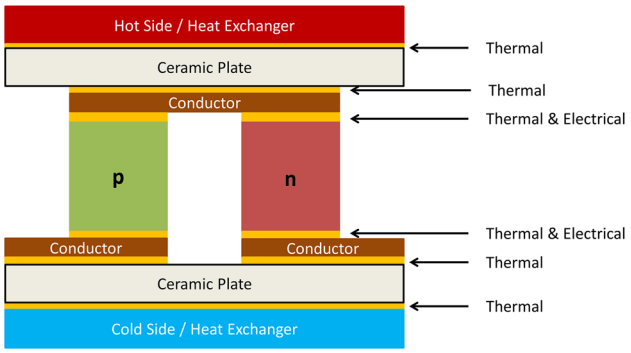

Fig. 1. Location of thermal and electrical contacts in a thermoelectric couple.

on a thermoelectric material that is well suited for large-scale waste heat harvesting applications.[13] The Fe_2VAl compound, first studied by Nishino et al.,[14–16] is based on low-cost elements and exhibits a high power factor (up to 6.8×10^{-3} W m K^{-2}). Moreover, adequate doping or decrease of the grain size can significantly decrease its thermal conductivity, leading to ZT values of around 0.2 in the range of 400 K to 500 K.[17,18] Finally, the processing and manufacturing properties of Fe_2VAl compounds are very close to those of metallic materials, representing a great advantage for large-scale applications.

Different joining techniques were tested and characterized by looking at both the microstructure and the resulting electrical properties. The resulting performance of fully working prototypes is discussed using a lumped model that highlights the relationship between the microstructure and system performance, providing guidelines for enhancement of system performance.

EXPERIMENTAL PROCEDURES

Thermoelectric Materials

The Fe_2VAl thermoelectric material used in this work was processed by induction melting of ferrovanadium, iron, and aluminum pellets followed by a slow cooling stage (10 K min^{-1}) to avoid cracking or solidification defects. Ferrovanadium was used instead of pure vanadium because of its much lower cost without degrading the thermoelectric performance. The doping strategy is based on off-stoichiometric optimization according to the formula $(Fe_{2/3}V_{1/3})_{100-y}Al_y$. Indeed, varying the aluminum concentration allows a switch from n- to p-type material.[14] Amounts of each constituent required to achieve the correct stoichiometry were placed in a boron nitride crucible then heated up to 1960 K under vacuum during 20 min before being slowly cooled (10 K min^{-1}). The resulting ingots weighed around 100 g. The compositions of the base materials and the melted samples were compared. Slight loss (below 0.5 at.%) of Al and V was observed due to precipitation of nitrides and carbides.[19] Table I summarizes the actual compositions measured by inductively coupled plasma atomic emission spectroscopy. Boron nitride crucibles were used to limit C contamination during the melting process. Values below 0.15 wt.% C were measured on processed samples, which has been shown to have no influence on the Seebeck coefficient.[19]

Joining Processes

A good joint must present adequate chemical reactivity at the thermoelectric material–metal junction to achieve good mechanical strength while avoiding formation of brittle intermetallic compounds at the interface that would lead to higher surface contact resistivity.[1] Furthermore, it can be postulated that a smaller joint thickness will lead to a smaller surface contact resistivity. In this work, copper was selected for the metallic junctions, motivated by the fact that it has been previously demonstrated that copper can perform up to 673 K and resist thermal cycling in Fe_2VAl-based TEGs.[20,21]

Different joining solutions were applied on 0.7-mm-thick copper sheets. Fe_2VAl samples were machined into 5 mm × 5 mm × 5 mm cubes. Copper and Fe_2VAl were slightly polished with SiC paper and degreased with ethanol before each joining process. Four different techniques were tested to join the thermoelectric Fe_2VAl blocks with copper connecting sheets: conductive silver glue, tin solder, silver braze, and diffusion-bonded copper. In contrast to commercial thermoelectric modules, in which solders based on tin-bismuth alloys are widely used,[9] other techniques were studied here, since the nature of the materials and the expected

Table I. Characteristics of prototypes

	p-Type			*n*-Type			
Prototype	**Composition**	**S (μV K^{-1})**	**ρ ($\mu\Omega$ m)**	**Composition**	**S (μV K^{-1})**	**ρ ($\mu\Omega$ m)**	**Leg Size (mm^3)**
Ag glue	$Fe_{49.2}V_{24.3}Al_{26.5}$	42	1.47	$Fe_{52.6}V_{25.4}Al_{22.6}$	−20	8.77	5 × 5 × 5
Sn solder	$Fe_{50.9}V_{24.7}Al_{24.4}$	72	4	$Fe_{51.7}V_{26.1}Al_{22.2}$	−70	5.8	4.3 × 5 × 5
Ag braze	$Fe_{50.9}V_{24.7}Al_{24.4}$	72	4	$Fe_{51.7}V_{26.1}Al_{22.2}$	−70	5.8	4.3 × 5 × 5
Diffusion bonded	$Fe_{49.3}V_{23.7}Al_{27}$	71	2.32	$Fe_{52.8}V_{26.4}Al_{20.8}$	−97	4.77	4.2 × 4 × 4

operating temperature range (up to 673 K[13]) are significantly different. Even though they cannot reach such high temperatures, silver glue and tin solder were tested since they are quite conventional solutions that are widely used in other applications.[22] Silver brazing has been successfully used for iron aluminide joining.[23] Since it provides low wetting angles, this technique seemed promising for Fe_2VAl-Cu joining. Since copper presents good wetting behavior with iron aluminides,[24] direct joining of copper to Fe_2VAl using a diffusion-bonding technique was also considered. Furthermore, this process was used previously by Mikami et al.[20]

The silver glue was an epoxy-based glue containing micrometric silver particles. The glue used in this work was 10HT/S from MasterBond with intrinsic electrical resistivity below 2 $\mu\Omega$ m and working temperature range of 4 K to 477 K. It was deposited by hand using a spatula. The curing stage consisted in holding for 45 min at 418 K under ambient atmosphere. The Fe_2VAl-Cu assembly was furthermore pressed using a screwed assembly.

The tin solder used in this study, commercialized by Multicore, was solder paste with composition of 95.5 wt.% Sn, 3.8 wt.% Ag, and 0.7 wt.% Cu, having a melting point around 490 K. The soldering cycle was carried out with a holding time of 20 min at 540 K under ambient atmosphere in the same clamping assembly used for the silver glue.

The silver braze used was 1666PA from Castolin with composition of 45 wt.% Ag, 27 wt.% Cu and 28 wt.% Zn and liquidus and solidus temperatures of 953 K and 913 K, respectively. The brazing cycle was conducted under vacuum (0.1 mbar) at 973 K for 15 min in a SRO-700 furnace from ATV Technologie.

For diffusion bonding of Fe_2VAl and copper, the Fe_2VAl sample was pressed under 20 MPa between two copper sheets and heated at 50 K min^{-1} to 1200 K for 2 min in a spark plasma sintering (SPS) device (HPD10, FCT Systeme).

Characterization of the Joints

The microstructure of the joints was characterized by scanning electron microscopy (SEM) and energy-dispersive x-ray spectroscopy (EDX). The Fe_2VAl-Cu assemblies were cut transversally to the interface before being polished to observe the interface between copper and Fe_2VAl.

The total electrical resistance of the different joined samples, R_{meas}, was measured using a custom four-probe setup. Knowing the internal resistance of the Fe_2VAl sample, the R_{mat} derived from its geometry, and the material electrical resistivity, the electrical contact resistivity ρ_{sc} in $\Omega\ m^2$ can be estimated as

$$\rho_{sc} = (R_{meas} - R_{mat})A, \quad (1)$$

where A is the contact area of the Fe_2VAl sample (25 mm^2 in this work).

This method is similar to the integral method proposed and validated by De Boor et al.[4]

Processing of Prototypes

Four prototypes were fabricated based on different Fe_2VAl compounds and different joining techniques with a number of couples varying from 7 to 40. The lower copper plates were first properly placed in an array, on which a layer of joining material was deposited. The *p*-type legs were then placed, followed by the *n*-type legs (or alternatively), then a layer of joining material was deposited on these legs. Finally, the upper copper plates were placed. Each prototype used copper plates of 5 mm × 12 mm × 0.7 mm. The different prototypes were:

- **A silver glue prototype** For the assembly of this first prototype, a droplet of silver glue was placed on each Cu-Fe_2VAl interface by hand. Once the assembly was completed, it was heated up to 418 K for 45 min under ambient air.
- **A tin soldering prototype** This second prototype was designed using the same scheme as the silver glue prototype. Owing to the larger number of couples with higher Seebeck coefficient and better electrical contact, better performance was expected from this prototype. The same steps as for the silver glue prototype were carried out with a heating stage at 540 K for 20 min.
- **A silver brazing prototype** This prototype was designed to work at higher temperatures than the previous ones using the same Fe_2VAl compounds. For this prototype, the assembly was carried out on a graphite PAPYEX sheet (from MERSEN) in a SRO-700 furnace and an alumina plate was put on top of it. To ensure good contact, pressure of 17 kPa was applied on top of the assembly using a weight. The brazing cycle was carried out at 973 K for 15 min.
- **A copper diffusion-bonded prototype** The Fe_2VAl legs were joined to copper using the diffusion bonding technique previously presented. The assembly was then been carried out with silver brazing and pressure for copper–copper junctions as for the previous prototype.

The materials and geometrical properties of these prototypes are detailed in Table II. The geometry of the thermoelectric legs was chosen to facilitate the machining process and manual manipulation during prototype assembly.

Measurements of the Performance of the Prototypes

Two types of measurement were carried out on the prototypes. Firstly, the internal electrical resistance (R_{meas}) was measured using a four-probe

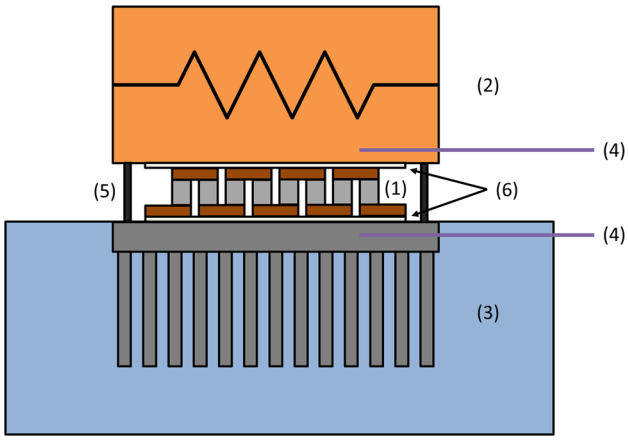

Fig. 2. Schematic representation of custom setup used for module characterization: 1, module; 2, heater sheeted with anodized aluminum; 3, heat sink made of anodized aluminum immersed in a cooled propanol bath; 4, thermocouples; 5, clamping screws; 6, thermal grease layers.

technique. Small currents (≤ 100 mA) were used to minimize the influence of the thermoelectric effect on the measurements. Secondly, the open-circuit voltage (V_{oc}) for a given temperature difference between the cold and hot sides of the TEG was measured on the custom setup shown schematically in Fig. 2. In this setup, a finned heat sink is immersed in a controlled cooler, allowing temperatures down to 233 K. The prototype is placed between the heat sink and an electrical heater (a 1 Ω, 200 W rated power resistance) allowing heating of the hot side up to 423 K. The heat sink and heater casing were both made out of anodized aluminum. The anodized layers serve as insulators between the copper plates and heat exchangers and avoid the use of additional ceramic plates. Silicon thermal grease was used on both sides of the prototype to ensure good thermal contact. Screws were used to clamp the prototypes between the heater and heat sink to add some pressure and ensure good contact. Holes were drilled in the heat sink and the aluminum casing of the heater to measure the hot- and cold-side temperatures using K-type thermocouples. Voltage was measured with a portable multimeter. Note that the silver glue prototype was assembled and screwed between the heater and heat sink before the curing step.

Based on the measured open-circuit voltage and corresponding temperature difference, the effective Seebeck coefficient proposed by Huang et al.[25] can be deduced using the following equation:[26]

$$V_{oc} = \sum_{mat} \Delta T_{teg} = \sum_{meas} \Delta T, \tag{2}$$

where V_{oc} is the open-circuit voltage, $\sum_{mat} = S_p - S_n$ is the Seebeck coefficient of the material couple in V K^{-1}, ΔT_{teg} is the effective temperature difference across the thermoelectric legs, $\sum_{meas}$ is the

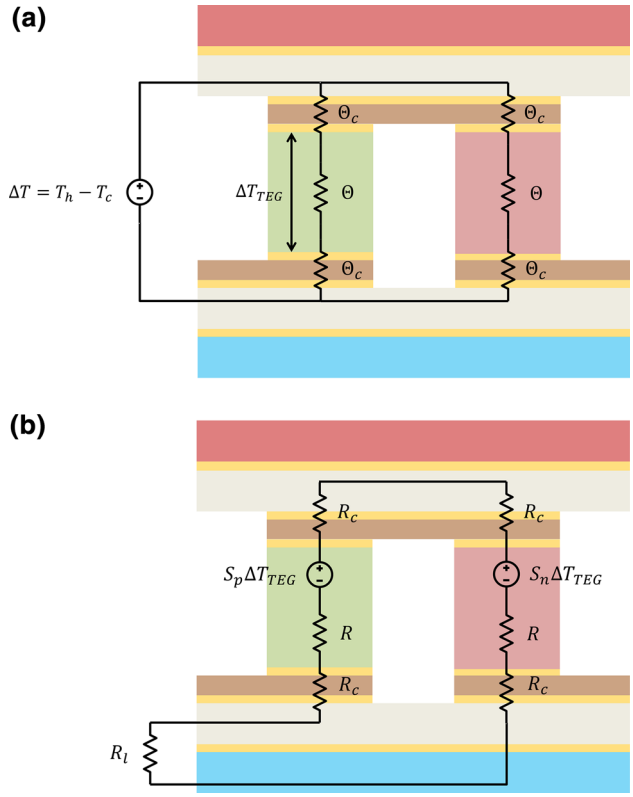

Fig. 3. (a) Description of thermal lumped model. (b) Electrical lumped model used to assess the properties of the prototypes.

effective Seebeck coefficient, and ΔT is the temperature difference measured across the prototype.

Lumped Model of Thermoelectric Prototypes

To critically assess the influence of the thermal and electrical contact resistances, a first-order lumped model was developed. This model easily computes the electrical power generated by a TEG considering the contact resistances, besides the thermoelectric material properties and generator geometry. This model is composed of two uncoupled subcircuits. The thermal subcircuit (Fig. 3a) computes the effective temperature difference between the extremities of the thermoelectric legs, ΔT_{teg}. In this subcircuit, the thermal resistance of the thermoelectric leg, Θ, and the thermal contact resistance, Θ_c, in K W^{-1}, are defined by Eqs. 3 and 4, respectively:

$$\Theta = \frac{l}{kA}, \tag{3}$$

$$\Theta_c = \frac{r_{sc}}{A}, \tag{4}$$

where l is the thermoelectric leg length, A is the thermoelectric leg area, k is the mean thermal

conductivity of the thermoelectric material in W m^{-1} K^{-1}, and r_{sc} is the thermal contact resistivity in K m^2 W^{-1}. From the definition of these resistances and knowing the temperature difference between the heat source and sink, ΔT, the effective temperature difference on the thermoelectric legs can be computed as

$$\Delta T_{teg} = \Delta T \frac{\Theta}{2\Theta_c + \Theta}. \quad (5)$$

Equation 5 can be rewritten to describe the relative temperature difference as a function of the thermal parameters as follows:

$$\frac{\Delta T_{teg}}{\Delta T} = \frac{1}{1 + 2\frac{r_{sc}k}{l}}. \quad (6)$$

The electrical subcircuit (Fig. 3b) is used to estimate the electrical power generated by the TEG. The total TEG resistance is defined as

$$R_{teg} = R_p + R_n + 4R_c = \frac{\rho_p l}{A} + \frac{\rho_n l}{A} + 4\frac{\rho_{sc}}{A}, \quad (7)$$

where ρ_p *and* ρ_n are the electrical resistivity of the thermoelectric materials in Ω m and ρ_{sc} is the electrical contact resistivity in Ω m^2. The open-circuit thermoelectric voltage can be computed from ΔT_{teg} and $\sum_{mat}$ using Eq. 2.

Knowing R_{teg} and V_{oc}, the electrical power at matched load, P_{max}, can be computed as

$$P_{max} = \frac{V_{oc}^2}{4R_{teg}}. \quad (8)$$

Using Eq. 2, the power can be expressed as

$$P_{max} = \frac{\left(\sum_{mat} \Delta T_{teg}\right)^2}{4R_{teg}}. \quad (9)$$

The present model assumes temperature-independent properties and neglects the physical coupling occurring through the Joule, Peltier, and Thomson effects. These strong assumptions are valid for a first-order approximation.[27]

RESULTS

Microstructure of the Joints

The interface of Fe_2VAl assembled to Cu with silver glue is shown in Fig. 4. Silver particles and the epoxy matrix can be discriminated, showing that the conductive phase did not completely fill the joint between Fe_2VAl and Cu. It is also worth noting that the silver glue layer has a width in the range of 10 μm to 20 μm.

Figure 5 shows the interface of the assembly using the tin solder. The global shape of the tin solder suggests very good wetting of Cu, but in contrast no wetting of Fe_2VAl. This explains the discontinuity of the interface between Fe_2VAl and

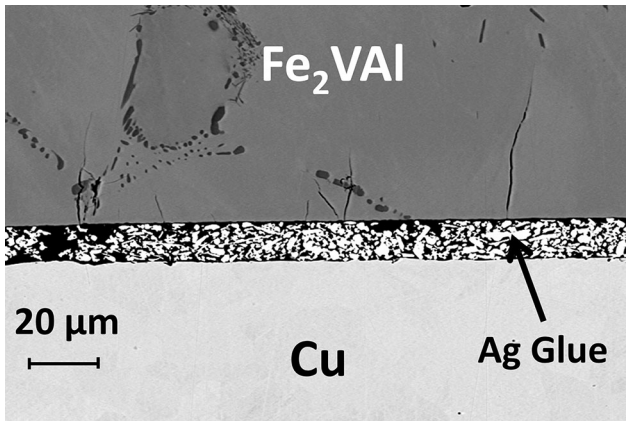

Fig. 4. Micrograph of cross-section of Fe_2VAl–silver glue–Cu assembly.

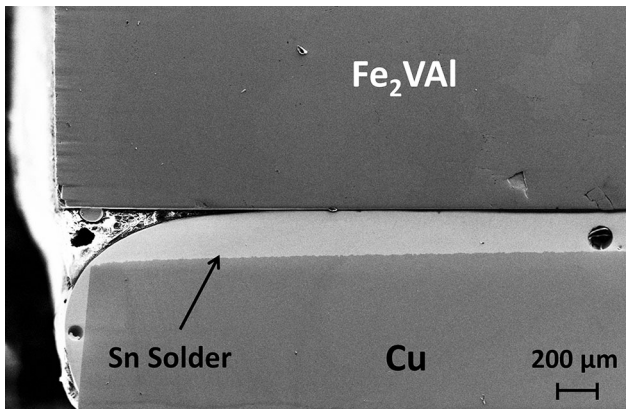

Fig. 5. Micrograph of cross-section of Fe_2VAl–tin solder–Cu assembly.

solder and the large contact resistivity reported in the next section, as well as the weak mechanical strength. Indeed, Fig. 6 shows the Fe_2VAl soldered sample after disassembly of the Cu–Fe_2VAl joint. It is clear from Fig. 6a that the tin solder joint is quite ineffective. The major part of the surface is free of solder. Moreover, there are some zones free of tin solder inside the solder droplet, leading to an even smaller effective contact surface, as highlighted at higher magnification in Fig. 6b.

Figure 7a shows the complete Fe_2VAl–Cu interface when joined with silver braze. It can be observed that only one-third of the total interface was really connected by the braze. On the other hand, when zooming in on the interface, it is clear that the braze reacted with copper. On the Fe_2VAl side, there did not seem to be any reactivity at this scale. The chemical composition profile in Fig. 7b highlights that the reactive layer on the Cu side is composed of 70 at.% Cu, 20 at.% Zn, and up to 10 at.% Ag, similar to that of the Cu-rich particles present in the brazed joint. Figure 8 shows the Fe_2VAl surface after disassembly of the specimen. Figure 8a reveals that the surface was still mostly

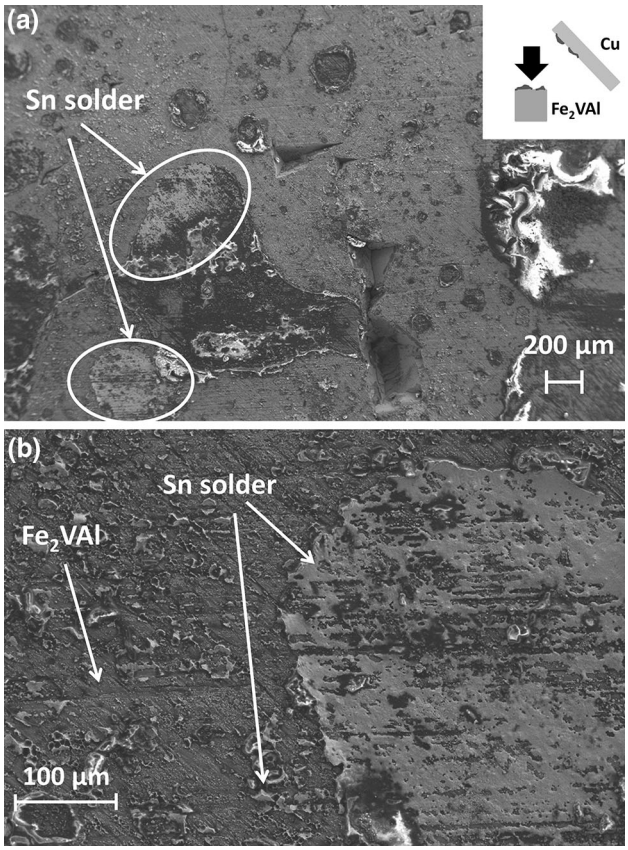

Fig. 6. (a) Micrograph of Fe_2VAl surface after disassembly of the tin soldered specimen. (b) Magnified view on a tin droplet of (a).

covered by the silver braze, as seen even more clearly at higher magnification in Fig. 8b. This may indicate that some reaction may have occurred between the braze and Fe_2VAl, although a reaction layer could not be observed in this work.

Figure 9 presents a SEM micrograph and EDX profile of the diffusion-bonded joint. The micrograph in Fig. 9a shows the presence of a thin zone where copper reacts with Fe_2VAl. When zooming in, it becomes clear that diffusion of copper occurred along Fe_2VAl grain boundaries close to the interface. The chemical profiles in Fig. 9b show that the bright-grey zone at the interface is depleted in aluminum. This depleted zone is about 5 μm, with some copper particles located in this zone. The profile shows that aluminum also diffused within the copper layer.

Characterization of Electrical Contact

The measured electrical contact resistivities are presented in Fig. 10 for the different joining techniques, varying in a very large range depending on the joining process, from $9.46 \times 10^{-6}\ \Omega\ m^2$ for the silver glue down to $5 \times 10^{-9}\ \Omega\ m^2$ for the silver braze and diffusion-bonded copper.

Prototypes

Table II summarizes the experimentally determined electrical characteristics (R_{meas} and Σ_{meas}) as well as the calculated ones (R_{mat} and Σ_{mat}; where the subscript "mat" relates to the material properties) estimated based on the geometry of the prototypes and properties of the materials. These characteristics are those expected in the absence of contact resistance. The measured internal resistance decreased drastically from 40,000 mΩ for the Ag glue prototype down to less than 50 mΩ for the Ag braze and diffusion-bonded Cu prototypes, while the effective Seebeck coefficient varied by a factor of around 5. This is mainly due to the fact that the internal resistance is directly linked to the electrical contact resistance, which varied significantly with the joining technique applied (see previous section), while the effective Seebeck coefficient is not directly linked to the electrical contact resistance.

DISCUSSION

Joining Processes

Högblom et al.[10] reported electrical contact resistivities in the range of $10^{-9}\ \Omega\ m^2$ to $10^{-7}\ \Omega\ m^2$ for TEGs, depending on the process applied. Most of the techniques used in this work are thus in the range of good performance, except for the tin solder and definitely the silver glue.

The high contact resistivity of the silver glue cannot be explained by its bulk resistivity ($\sim 2\mu\Omega$ m) nor the presence of large porosity (Fig. 4). A Cu-to-Cu joining test was carried out using the same conditions, and a low contact resistivity of $3.5 \times 10^{-9}\ \Omega\ m^2$ was measured. Therefore, the origin of the large contact resistivity is probably the silver glue–Fe_2VAl interface. The presence of a very thin layer of alumina on the Fe_2VAl could explain this large contact resistivity, as reported by Weidler et al. in the case of aluminum–silver glue contacts.[22]

In the case of the tin solder, Ebling et al.[9] reported a similar contact resistivity (up to $1.72 \times 10^{-8}\ \Omega\ m^2$) from soldering tests on Bi_2Te_3 with Sn-Ag-Cu solder. This level of contact resistivity could be explained by the poor wetting behavior and weak strength of the joint between Fe_2VAl and tin solder (Figs. 5, 6).

The process leading to the smallest contact resistivity (diffusion bonding) exhibits a specific reactivity and the creation of a smooth interphase transition between Fe_2VAl and Cu. In this process, diffusion of aluminum in copper is highlighted, which can be explained by two phenomena: (1) aluminum presents the largest diffusion coefficient, and (2) looking at the phase diagrams of the Al–Cu, Fe–Cu, and V–Cu couples, Al presents a large solubility in Cu,[28] indicating good chemical affinity between these two elements.

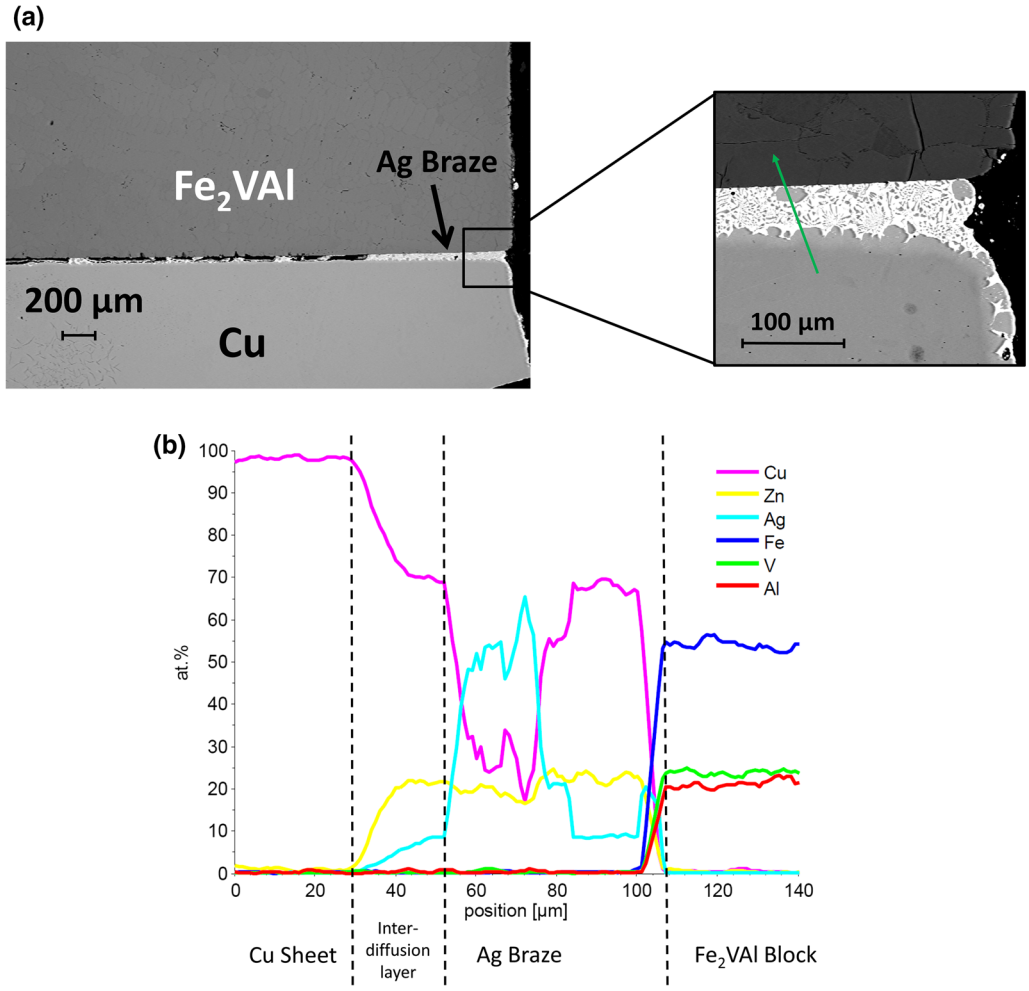

Fig. 7. (a) Micrograph of silver brazing test. (b) EDX chemical profile across the interface, along the green arrow in (a) (Color figure online).

Figure 10 also shows that silver brazing exhibited electrical contact resistivity similar to that of copper diffusion bonding (in the $10^{-9}\ \Omega\ m^2$ range). Comparing the interface of the tin solder test (Fig. 5) and the silver brazing test (Fig. 7b), it is obvious that the silver braze presented a lower contact angle on Fe_2VAl than the tin solder, which could indicate better wetting of the silver braze. This may explain the lower contact resistivity, despite the high porosity in the silver braze joint and the similar bulk resistivities of the filler materials (about $10^{-7}\ \Omega$ m). Indeed, the contribution of the silver braze (considering that one-third of the area is effectively joined) is around $5.5 \times 10^{-11}\ \Omega\ m^2$, still two orders of magnitude lower than the measured electrical contact resistivity. The better joining behavior of silver braze compared with tin solder is also confirmed by the disassembled surfaces (Figs. 6, 8). Indeed, the Fe_2VAl surface covered with silver braze is much larger than in the case of tin solder.

Considering the contact resistivities and ease of implementation, silver brazing and diffusion bonding seem to be the most suitable techniques for development of effective prototypes.

Assembly of Prototypes

Based on the theoretical and experimental values and taking into account the geometrical configurations of the different prototypes, the following three contact parameters presented in Table III can be estimated:

- **The mean electrical contact resistivity** ρ_{sc} for the prototype can be computed as

$$\rho_{sc} = \frac{(R_{meas} - R_{mat})}{4N} A, \tag{10}$$

where A is the thermoelectric leg area and N is the number of thermoelectric couples in the prototype. The factor of 4 is due to the number of contacts per couple (2 per leg).

- **The Seebeck ratio**, Σ_{ratio} defined as[25]

$$\sum_{ratio} = \frac{\sum_{meas}}{\sum_{mat}}; \tag{11}$$

- **The thermal contact resistivity,** r_{sc} can be computed by using the Seebeck ratio. From

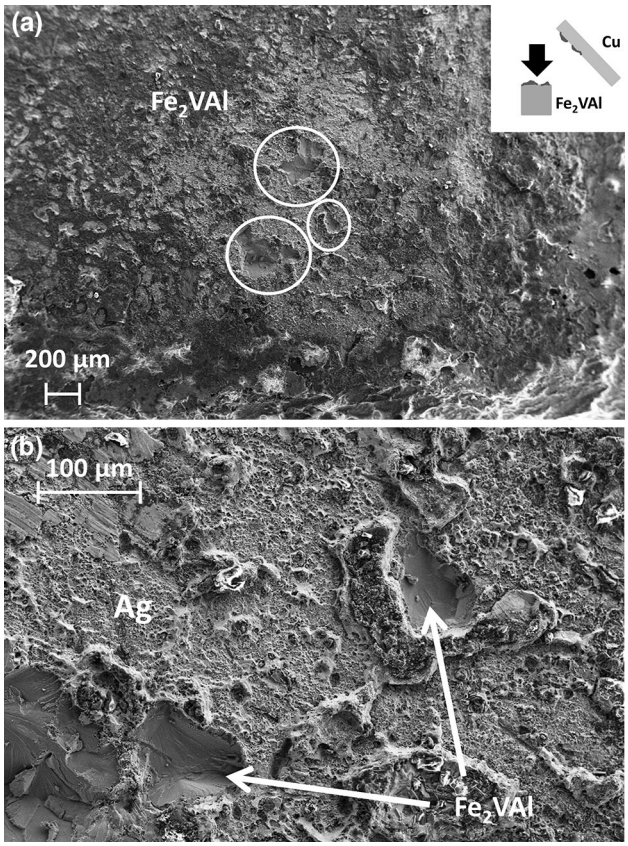

Fig. 8. (a) Micrograph of Fe_2VAl surface after disassembly of the silver brazed specimen. (b) Magnified view of the silver-free zone in (a).

Eqs. 2, 6, and 11, it can be written as

$$\sum_{\text{ratio}} = \frac{\Delta T_{\text{teg}}}{\Delta T} = \frac{1}{1 + 2\frac{r_{\text{sc}}k}{l}}. \tag{12}$$

Rewriting this equation, the thermal contact resistivity can be expressed as

$$r_{\text{sc}} = \left(\sum_{\text{ratio}}^{-1} - 1\right)\frac{l}{2k}. \tag{13}$$

It is worth noting that the thermal conductivity of the thermoelectric material and the thermoelectric leg length must be known. A mean thermal conductivity of 12.5 $W\,m^{-1}\,K^{-1}$ taken from literature[29] was used for the Fe_2VAl samples processed in this work.

Σ_{ratio} is dependent on the geometry. Indeed, longer thermoelectric legs result in an increase of this ratio for the same thermal contact resistance, which means that it can only be used to compare TEGs with the same geometry. On the other hand, the electrical and thermal contact resistivities are independent of the module geometry and can be used to compare different prototypes. For the sake of comparison, the characteristics and performance of two Fe_2VAl-based modules reported in literature (from the works of Mikami et al.[20,21] on Ti, Si, and W doping) are also presented in the final two rows of Table III.

The mean electrical contact resistivity values determined for the prototypes are in reasonable agreement with those measured previously during the characterization of the individual joints (Fig. 10). Only in the case of the silver glue is an overall value significantly higher (about 176%) than that of the single test obtained. Hence, except in the latter case, all the prototypes exhibited good electrical contact resistivity in the range of values reported in literature ($10^{-9}\ \Omega\,m^2$ to $10^{-7}\ \Omega\,m^2$).[10] When looking at the electrical contact resistivities of the two last prototypes, it is obvious that the use of silver braze ensures a low electrical contact resistivity. Meanwhile, the diffusion-bonded prototype presented nearly the same electrical contact resistivity as the silver braze prototype, confirming that Cu–Fe_2VAl joints present ultralow resistivity.

To highlight the contribution of the silver braze in this assembly, a copper-to-copper joint was silver brazed. The measured contact resistivity was $1.7 \times 10^{-9}\ \Omega\,m^2$, representing about 40% of the total surface contact resistivity of the Fe_2VAl/Cu/Braze/Cu assembly. This conclusion is confirmed when looking at the two state-of-the-art prototypes from Mikami et al.[20,21] that exhibited electrical contact resistivity one order of magnitude lower than in this work. This lower contact resistivity probably results from the fact that they manufactured the prototypes only by SPS (without an additional brazing step). Further work on the scalability of this process and the resulting mechanical properties should be considered.

The Seebeck ratio, Σ_{ratio}, of all the prototypes lay in the range of 0.4 to 0.7, which is comparable to other works (Table III). As defined in Eq. 12, this ratio depends on the thermal contact resistance and the thermal resistance of the thermoelectric leg. Therefore, a higher Seebeck ratio will be obtained when lowering the thermal contact resistivity or thermoelectric leg thermal conductivity and when increasing the thermoelectric leg length. These effects are highlighted when comparing the silver glue prototype with the others (Table III).

For the thermal contact, the first prototype presented the lowest thermal contact resistivity. This can be explained by the fact that the silver glue prototype was assembled between the heater and heat sink used for the characterization before the curing step. Therefore, its planarity could have been improved compared with other modules, leading to lower thermal contact resistance. A typical thermal contact value of about $2 \times 10^{-4}\ K\,m^2\,W^{-1}$ was found for the other prototypes, similar to the value found by Hogblöm et al.[10] for commercial bismuth telluride modules.

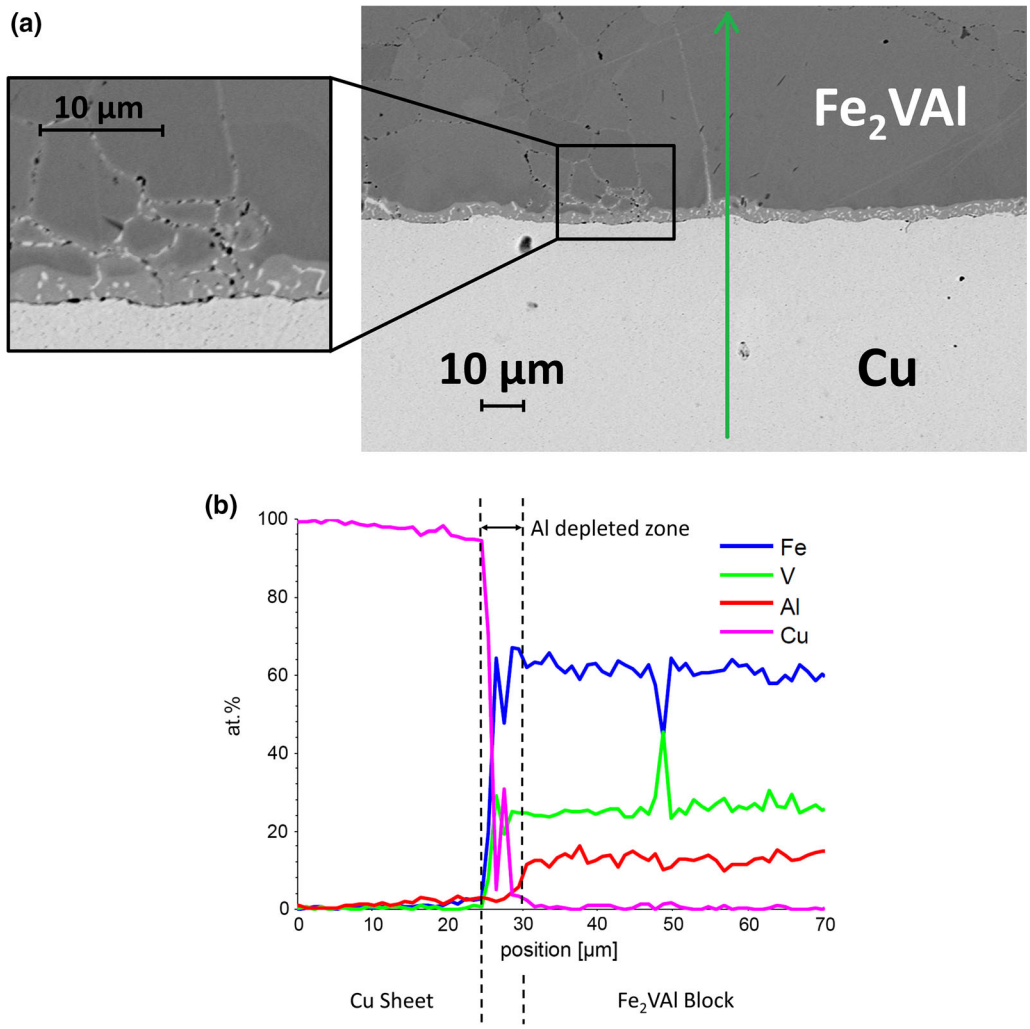

Fig. 9. (a) Micrograph of interface of diffusion bonding test. (b) EDX chemical profile across interface, following the green arrow in (a) (Color figure online).

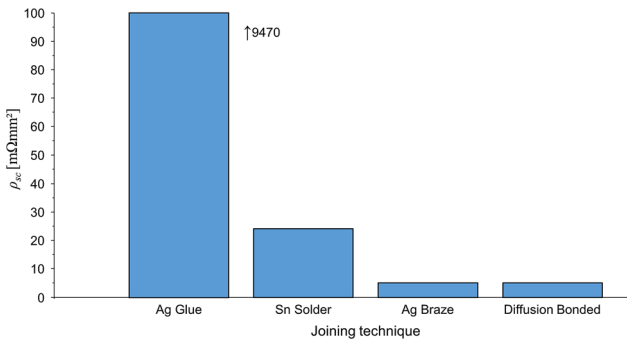

Fig. 10. Surface electrical contact resistance measured during joint testing for four different joining techniques.

Finally, the two state-of-the-art prototypes from Mikami et al.[20,21] present similar thermal contact characteristics to the present work. This may indicate that the thermal contacts are dominated by the interface (anodized aluminum and thermal grease in this work) between the copper plates and heat source and sink rather than by the interface between copper and thermoelectric materials.

Several performance indexes of the prototypes were computed from the measurements described above. To compare the different prototypes, together and with respect to literature, Table III presents the following characteristics:

- $P_{\max}$, the power at matched load for a 200 K temperature difference, estimated as

$$P_{\max} = \frac{\left(\sum_{\text{meas}} \Delta T\right)^2}{4R_{\text{meas}}}; \tag{14}$$

- $p_{\max/\text{mat}}$, the resulting power density based on the thermoelectric material area;
- $p_{\max/\text{tot}}$, the resulting power density based on the total area of the prototype.

Figure 11 presents the electrical contact resistivity, thermal contact resistivity, and total power density for the different prototypes and for those reported in

Table II. Measured properties of four prototypes

Prototype	R_{meas} (mΩ)	$\sum_{meas}$ (μV K^{-1})	R_{mat} (mΩ)	$\sum_{mat}$ (μV K^{-1})
Ag glue	40,000	620	30.7	920
Sn solder	255	2600	67.4	5680
Ag braze	45	494	32.7	994
Diffusion bonded	48.5	1125	29.8	2688

Table III. Characteristics and performance of prototypes for ΔT = 200 K

	Contact Properties			Power Performance		
Prototype	ρ_{sc} (Ω m^2)	$\sum_{ratio}$ (−)	r_{sc} (K m^2 W^{-1})	P_{max} (W)	$p_{max/mat}$ (W m^{-2})	$p_{max/tot}$ (W m^{-2})
Ag glue	1.67×10^{-5}	0.67	9.85×10^{-5}	9.61×10^{-5}	0.128	0.107
Sn solder	2.93×10^{-8}	0.46	2.02×10^{-4}	0.265	132.5	110.41
Ag braze	4.80×10^{-9}	0.50	1.72×10^{-4}	5.42×10^{-2}	67.75	56.46
Diffusion bonded	4.58×10^{-9}	0.42	2.32×10^{-4}	0.261	509.77	407.81
Fe_2VAl[20]	3.27×10^{-10}	0.42	2.89×10^{-4}	0.486	687	397
Fe_2VAl W[21]	8.33×10^{-11}	0.75	7.14×10^{-5}	0.715	4965	2474

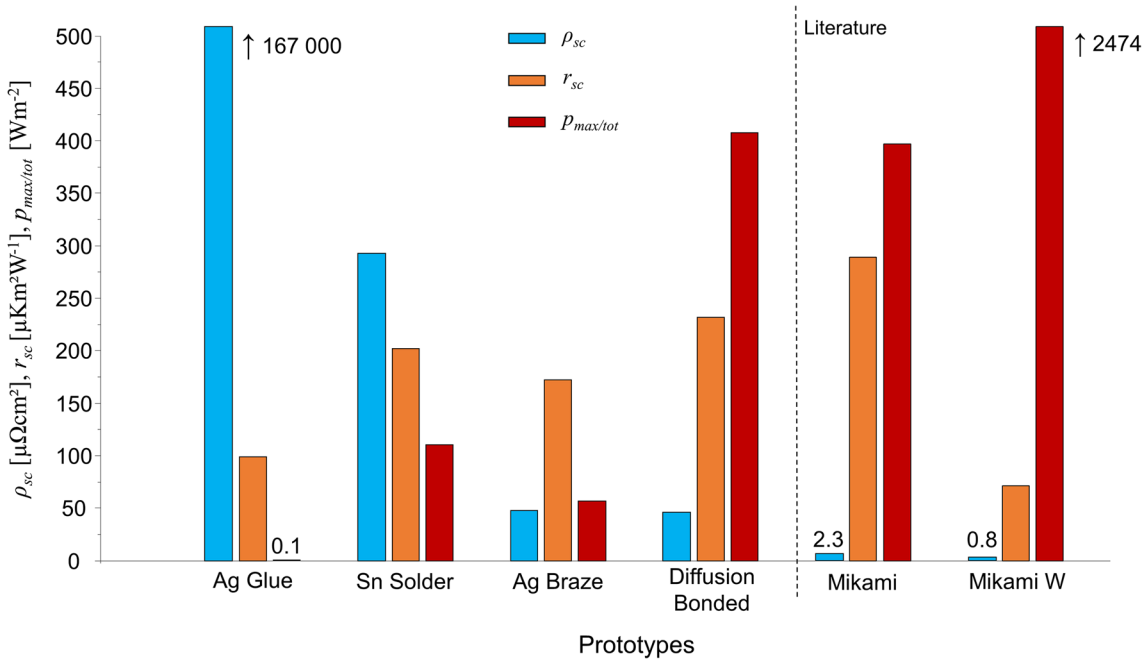

Fig. 11. Performance and contact characteristics of prototypes: ρ_{sc} in $\mu\Omega$ m^2 (blue bars), r_{sc} in μK m^2 W^{-1} (orange bars), and total power density in W m^{-2} (red bars). The characteristics of two prototypes were estimated using data from literature for the sake of comparison: a Si/Ti-doped ("Mikami" from Ref. 20) and a W-doped device ("Mikami W" from Ref. 21) (Color figure online).

literature. From this graph, it is clear that the dramatic decrease of the electrical surface contact resistivity thanks to the optimization of the joining process leads to a sharp increase of the power density.

It is worth noting that the best prototype of the present study presents similar performances to the Si/Ti-doped module of Mikami et al., which can be considered as the best result ever reported for a TEG based on Fe_2VAl. However, the present prototype is the first to be based on off-stoichiometric Fe_2VAl compounds. Furthermore, similar performances were achieved even with higher ρ_{sc}. Moreover, avoiding the use of doping elements and the powder metallurgy route allows faster production of modules at lower cost. Moreover, comparing this work with literature reveals that the relative difference between $p_{max/mat}$ and $p_{max/tot}$ is much

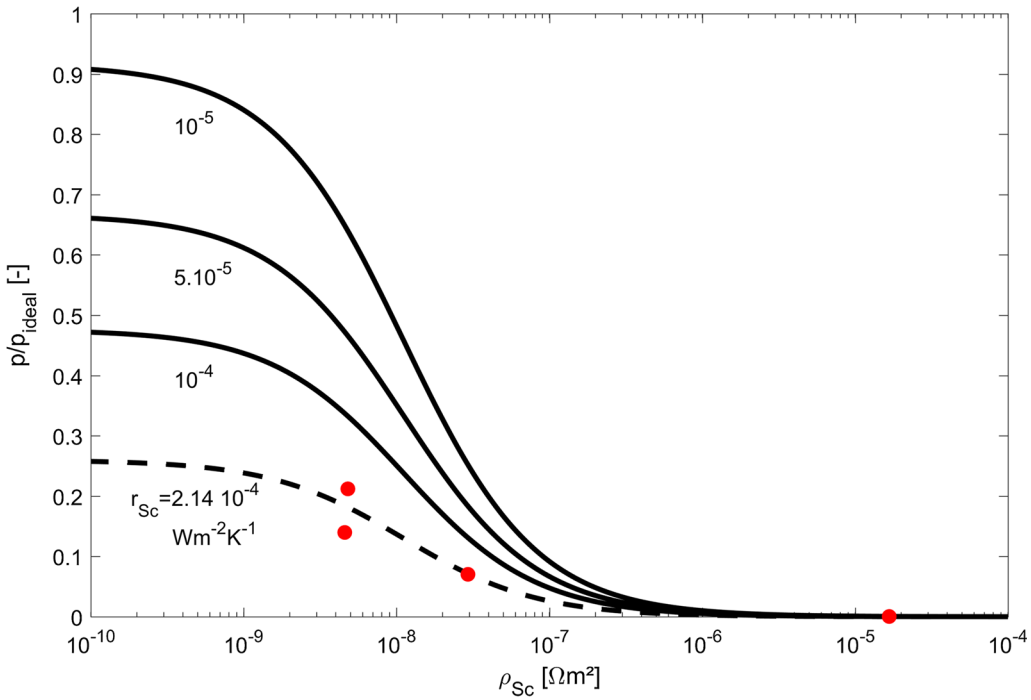

Fig. 12. Normalized power as function of electrical surface contact resistivity for different levels of thermal surface contact resistivity. Red dots correspond to different prototypes manufactured in this work. Black lines were computed with the lumped model using the following characteristics: ΔT = 200 K, l = 4.45 mm, k = 10 W m^{-1} K^{-1}, ρ = 5 $\mu\Omega$ m, and $S_p = |S_n|$ = 64.25 μV K^{-1}. The discontinuous black line was computed using the mean value of the thermal surface contact resistivities of the prototypes (Color figure online).

smaller in the present work than in the work of Mikami et al.,[20,21] indicating that the geometry used in this work is closer to optimal.

Optimization Based on Lumped Model

The influence of contact resistances on the delivered power can be highlighted using the lumped model. An example for ΔT = 200 K using Fe_2VAl as the thermoelectric material was computed. Figure 12 shows the ratio of the real to ideal power (without contacts) as a function of the electrical contact resistivity for different levels of thermal contact resistivity. The different curves increase up to a maximum when the electrical contact resistivity is minimized. Even though this parameter was not the subject of the optimization procedure in the present study, the thermal contact resistivity should be minimized too, since the smaller the thermal contact resistivity, the larger the power, whatever the value of the electrical contact resistivity.

Finally, the successive improvements in the prototype design allowed an increase in the power density by a factor of about 4000 owing to a sharp decrease of the electrical contact resistivity (by about four orders of magnitude). This sharp increase is clearly in agreement with the model presented at the beginning of this work, as depicted in Fig. 12. In this figure, the experimental data (red dots) agree well with the lumped model (discontinuous line) computed using the mean values of the prototype characteristics (l = 4.45 mm, ρ = 5 $\mu\Omega$ m, $S_p = |S_n|$ = 64.25 μV K^{-1}).

Since the goal of generator design should be to reach a ratio p/p_{ideal} as close as possible to 1, it can be stated that the improvement of the electrical contacts achieved through this work is close to optimal. However, there is still room for improvement by optimizing the thermal contacts. Moreover, since this work focused only on the influence of the assembly process on the performance of the prototype, further performance enhancement could be obtained through geometrical optimization.

Selection of the Joining Process

After the selection of the appropriate metal electrode (thermal expansion matching, chemical and mechanical stability at working temperature, etc.), this global study can be used to define the selection procedure of a joining process for new thermoelectric materials. A flowchart for this procedure is shown in Fig. 13, comprising the following steps:

1. **To select a joining process that leads to a good metallurgical bond**, good wetting and a thin reaction layer should appear during joining, although diffusion at the working temperature must be avoided. Basic principles of physical chemistry and metallurgy compiled in

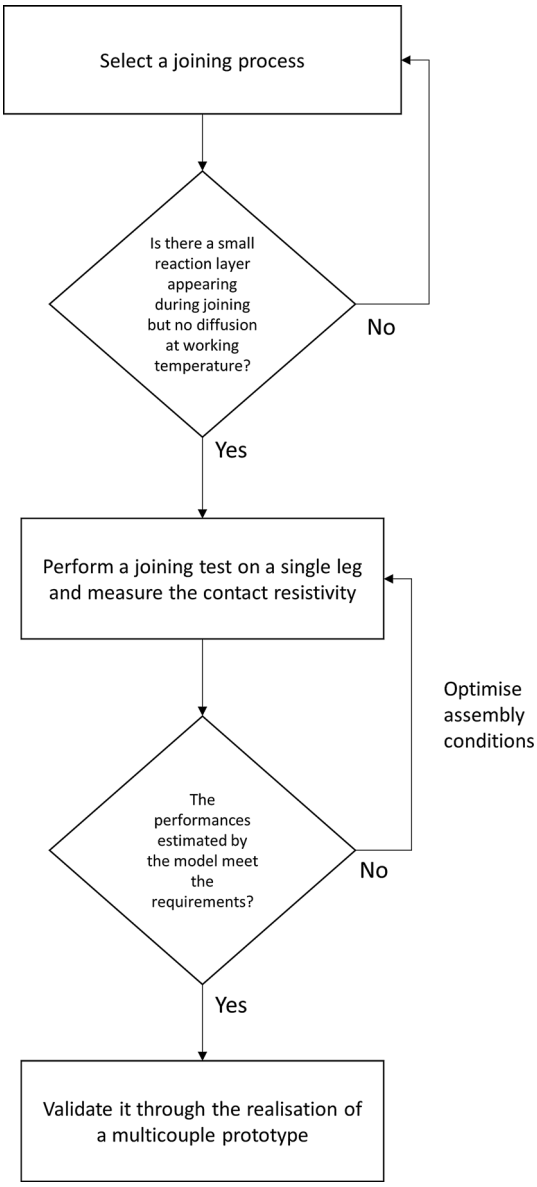

Fig. 13. Flowchart of selection of joining technique for high-performance TEGs.

tools such as phase diagrams, chemical affinity values, and microstructural characterization of the joint interface are the first required steps.

2. **To perform a joining test**, tests on single-leg samples should be used to determine joining conditions that lead to low electrical contact resistivity. A measurement setup for electrical contact characterization is required, as well as a model to estimate the performance.
3. **To assemble a multicouple working prototype**, the prototype should validate the upscaling of the joining technique, considering manufacturing and performance issues. The prototype should be fully characterized in terms of thermal and electrical contacts and performance.

It is mandatory that these different steps be fully completed to validate the choice of a joining process for development of thermoelectric generators using new thermoelectric materials. Therefore, the whole selection process should be taken into account when developing a joining process. Indeed, choosing a process that does not complete the three steps will definitely not lead to a high-performance generator. Such a choice is clearly illustrated by the silver glue example in this study, where no metallurgical bond occurred, leading to poor performance. In contrast, a good joining technique leading to good contact on single-leg samples could be developed, but fail to pass the upscaling stage towards the prototype assembly step by being too complex.

CONCLUSIONS

Thermoelectricity is a promising technology to change the way low-grade heat is considered. However, there is still room for improvement to bring this technology closer to real applications. In particular, thermal and electrical contacts should be minimized in TEGs to make full use of the potential of thermoelectric materials. A global assessment of these contacts is proposed herein.

The first-order lumped model described in this work allows easy estimation of the electrical power of a TEG considering the thermal and electrical contact resistivities. This model was used to highlight the influence of the contact resistivities on the electrical power density. The results show that these must be minimized to maximize the power density.

Based on the Fe_2VAl thermoelectric compound, a global analysis of the metal-to-thermoelectric material assembly was carried out. This analysis showed that assembly techniques leading to a reaction layer between the metal and thermoelectric material gave the lowest electrical contact resistivities.

Using these assembly techniques, several TEG prototypes were manufactured and characterized. The power density of the prototypes increased dramatically when using the best assembly techniques (by a factor of 4000 from the silver glue to the diffusion-bonded copper technique). Furthermore, these Fe_2VAl-based TEGs using the off-stoichiometric doping route are competitive with Si/Ti-doped prototypes[20] with power density above 500 W m^{-2} for a temperature difference of 200 K.

Future work should focus on simultaneous minimization of thermal and electrical contact resistivities in parallel with development of high-

performance, low-cost, and easily manufacturable thermoelectric materials. The selection process resulting from this study provides a simple and powerful tool to speed up such development.

ACKNOWLEDGMENTS

The authors acknowledge support from the Walloon Region through funding of the GTherm project. The European Regional Development Fund (ERDF) and Wallonia are also gratefully acknowledged for financial support of the research project (T-REX–EQUIDER - ECV12020010884F-830033) in the frame of the "Convergence programme."

REFERENCES

1. W. Liu, Q. Jie, H.S. Kim, and Z. Ren, *Acta Mater.* 87, 357 (2015).
2. D.M. Rowe and G. Min, *IEE Proc. A* 143, 351 (1996).
3. W. Liu, H. Wang, L. Wang, X. Wang, G. Joshi, G. Chen, and Z. Ren, *J. Mater. Chem. A* 42, 13093 (2013).
4. J. de Boor, C. Gloanec, H. Kolb, R. Sottong, P. Ziolkowski, and E. Müller, *J. Alloys Compd.* 632, 348 (2015).
5. D. Zhao, H. Geng, and L. Chen, *Int. J. Appl. Ceram. Tech.* 9, 733 (2012).
6. P. Ziolkowski, P. Poinas, J. Leszczynski, G. Karpinski, and E. Müller, *J. Electron. Mater.* 39, 1934 (2010).
7. R. Bjørk, *J. Electron. Mater.* 44, 2869 (2015).
8. B.V.K. Reddy, M. Barry, J. Li, and M.K. Chyu, *J. Heat Transf.* 136, 101401 (2014).
9. D. Ebling, K. Bartholomé, M. Bartel, and M. Jägle, *J. Electron. Mater.* 39, 1376 (2010).
10. O. Högblom and R. Andersson, *J. Electron. Mater.* 43, 2247 (2014).
11. H. Fateh, C.A. Baker, M.J. Hall, and L. Shi, *Appl. Energy* 129, 373 (2014).
12. P.H. Ngan, N. Van Nong, L.T. Hung, B. Balke, L. Han, E.M.J. Hedegaard, S. Linderoth, and N. Pryds, *J. Electron. Mater.* 45, 594 (2016).
13. G. Roy, E. Matagne, and P.J. Jacques, *J. Electron. Mater.* 42, 1781 (2013).
14. Y. Nishino, H. Kato, M. Kato, and U. Mizutani, *Phys. Rev. B* 63, 233303 (2001).
15. Y. Nishino and Y. Tamada, *J. Appl. Phys.* 115, 123707 (2014).
16. H. Miyazaki, S. Tanaka, N. Ide, K. Soda, and Y. Nishino, *Mater. Res. Express* 1, 015901 (2014).
17. M. Mikami, Y. Kinemuchi, K. Ozaki, Y. Terazawa, and T. Takeuchi, *J. Appl. Phys.* 111, 093710 (2012).
18. K. Renard, A. Mori, Y. Yamada, S. Tanaka, H. Miyazaki, and Y. Nishino, *J. Appl. Phys.* 115, 033707 (2014).
19. C. van der Rest, Ph.D. Thesis, Université catholique de Louvain (2015).
20. M. Mikami, K. Kobayashi, T. Kawada, K. Kubo, and N. Uchiyama, *J. Electron. Mater.* 38, 1121 (2009).
21. M. Mikami, M. Mizoshiri, K. Ozaki, H. Takazawa, A. Yamamoto, Y. Terazawa, and T. Takeuchi, *J. Electron. Mater.* 43, 1922 (2014).
22. Weidler, J. D., Burg, R. D., Decker, J. J., Constable, J. H, in *Proceedings of Electronic Components and Technology Conference* (2000), pp. 906–913.
23. R.K. Shiue, Y. Li, S.K. Wu, and L.M. Wu, *Metall. Mater. Trans. A* 41, 2836 (2010).
24. M. Brochu, M. Pugh, and R.A.L. Drew, *Intermetallics* 12, 289 (2004).
25. G.Y. Huang, C.T. Hsu, and D.J. Yao, *J. Electron. Mater.* 43, 2337 (2014).
26. C.T. Hsu, G.Y. Huang, H.S. Chu, B. Yu, and D.J. Yao, *Appl. Energy* 88, 5173 (2011).
27. M. Freunek, M. Müller, T. Ungan, W. Walker, and L.M. Reindl, *J. Electron. Mater.* 38, 1214 (2009).
28. H. Okamoto, M. Schlesigner, and E. Mueller, *ASM Handbook Volume 3: Alloy Phase Diagrams* (Materials Park: ASM International, 1992).
29. C.S. Lue, C.F. Chen, J.Y. Lin, Y.T. Yu, and Y.K. Kuo, *Phys. Rev. B* 75, 064204 (2007).